

Signatures of shape phase transitions in krypton isotopes based on relativistic energy density functionals

K. E. Karakatsanis^{1,2} and K. Nomura^{1,*}

¹*Department of Physics, Faculty of Science, University of Zagreb, HR-10000 Zagreb, Croatia*

²*Physics Department, Aristotle University of Thessaloniki, Thessaloniki GR-54124, Greece*

(Dated: July 1, 2022)

Spectroscopic properties that characterize the shape phase transitions in krypton isotopes with the mass $A \approx 80$ region are investigated within the framework of the nuclear density functional theory. Triaxial quadrupole constrained self-consistent mean-field calculations that employ relativistic energy density functionals and a pairing interaction are carried out for the even-even nuclei $^{76-86}\text{Kr}$. The spectroscopic properties are computed by solving the triaxial quadrupole collective Hamiltonian, with the ingredients, i.e., the deformation-dependent moments of inertia and mass parameters, and the collective potential, determined by using the SCMF solutions as microscopic inputs. Systematic behaviors of the SCMF potential energy surfaces, the corresponding low-energy spectra, electric quadrupole and monopole transition probabilities, and the fluctuations in the triaxial quadrupole deformations indicate evolution of the underlying nuclear structure as functions of the neutron number, that is characterized by a considerable degree of shape mixing. A special attention is paid to the transitional nucleus ^{82}Kr , which has been recently identified experimentally as an empirical realization of the E(5) critical-point symmetry.

I. INTRODUCTION

Quantum phase transitions (QPTs) are prominent phenomena in many areas of physics and chemistry. In the atomic nucleus, a class of QPT is suggested to occur between different intrinsic shapes in the ground state [1–6], which has been empirically identified as an abrupt change of observables along a given isotopic or isotonic chain with the addition or subtraction of only a few nucleons. A typical example is the phase transition from vibrational to rotational energy spectra around the neutron number $N = 90$ in the rare-earth region. The nuclear shape QPTs take place as functions of a discrete control parameter, i.e., nucleon number, hence an important question arises, as to how one can identify a particular nucleus as the critical point of the phase transitions. In addition, since the nuclei are finite quantum systems, the shape phase transitions are more or less smeared out in most of the realistic cases, which in turn points to another important question as to which physical observables can be regarded as the quantum order parameters of the phase transitions.

In the language of the interacting boson model (IBM) [7], the nuclear shape QPTs can be interpreted in terms of the transitions between different dynamical symmetries that emerge from the bosonic algebras, i.e., U(5), SU(3), and O(6) limits, which are associated with the spherical vibrational, deformed rotational, and γ -unstable rotational states, respectively. A different class of symmetry, referred to as the critical-point symmetry (CPS) was introduced in Refs. [8, 9], which provides a criterion to classify and interpret the nature of the collective states in transitional regions. This symmetry consists in exact

solutions of the geometric collective model that employs a potential appropriate for modeling the phase transition of interest. In particular, the E(5) CPS [8] corresponds to the transitional nuclei between the U(5) and O(6) limits, and is obtained analytically by solving the collective Schrödinger equation with a flat-bottomed potential characteristic of the U(5)-O(6) phase transition. The first empirical evidence for the CPS was suggested in the nucleus ^{134}Ba [10], where the low-energy spectrum and selection rules of the electric quadrupole transitions exhibit patterns predicted by the exact E(5) CPS. Numerous experimental investigations have been made to identify further evidence for the shape QPTs and the corresponding CPSs in wider ranges of the nuclear mass table, thus aiming to clarify whether the shape QPTs are ubiquitous phenomena in nuclear many-body systems. (see, e.g., Refs. [2, 11], and references are therein).

More recently, experimental evidence for the E(5) CPS has been suggested for the nucleus ^{82}Kr [12]. This would present a first empirical realization of the E(5) symmetry in the mass region $A \approx 80$, and extend the region of the critical-point phenomena to lighter mass regions that were hitherto not as extensively pursued as in the case of heavier nuclei. Empirically, the mass $A \approx 80$ nuclei around the Kr chain have also been suggested to demonstrate a rich variety of the nuclear structure phenomena, including the emergence of shape coexistence around the neutron sub-shell gap $N = 40$ [13–16]. Apart from the nuclear-structure point of view, the nucleus ^{82}Kr is also of particular interest, since it corresponds to the final-state nucleus of the possible neutrinoless double- β decay of ^{82}Se , and an accurate theoretical calculation for its low-lying states is useful for a reliable prediction of the nuclear matrix element of this decay process.

On the theoretical side, the nuclear shape QPTs and the related spectroscopic properties have been extensively studied from various approaches, including the al-

* knomura@phy.hr

gebraic models [2, 4, 6, 17, 18], the geometrical collective models [2, 6], the large-scale shell model [19–22], and the methods based on the nuclear density functional theory (DFT) [23–28]. In particular, the nuclear DFT framework has demonstrated an ability to provide an accurate, global, and computationally economical description of nuclear structure and dynamics [29]. Both relativistic [30, 31] and nonrelativistic [27, 32] energy density functionals (EDFs) have been successfully applied in the global description of the bulk nuclear matter and ground-state properties, as well as collective excitations, over the entire region of the nuclear mass chart. The EDF framework is basically implemented in the self-consistent mean-field (SCMF) calculations [33], in which an EDF is constructed as a functional of one-body nucleon density matrices that correspond to a single product state. To access spectroscopic properties, the EDF framework should be extended to take into account the dynamical correlations arising from the restoration of broken symmetries and fluctuations around the mean-field minima. A straightforward approach is the generator coordinate method (GCM) with symmetry projections and configuration mixing [27, 31–33]. In practical applications, the full GCM calculation in general becomes computationally demanding, especially in the case of heavy nuclei or when the large number of collective coordinates need to be taken into account. Alternative approaches to GCM have been provided, e.g., by the collective Hamiltonian [31, 34–36] and the mapped IBM [37, 38]. The EDF-based calculations both within the static and beyond SCMF approximations have also been extensively carried out to study the neutron-deficient Kr isotopes around the neutron sub-shell gap $N = 40$ (see, e.g., Refs. [39–46]).

Based on the relativistic EDF framework, here we investigate the evolution of the shape and low-lying states in the even-even Kr isotopes in the mass range $76 \leq A \leq 86$, particularly focusing on the proposed E(5) CPS around the transitional nucleus ^{82}Kr . The starting point is the triaxial quadrupole constrained SCMF calculations for the above Kr nuclei within the relativistic Hartree-Bogoliubov (RHB) framework [30, 31] using two representative classes of the relativistic EDF, i.e., the density-dependent meson-exchange (DD-ME2) [47] and point-coupling (DD-PC1) [48] interactions, and a separable pairing force of finite range [49]. Spectroscopic properties that can be considered signatures of the QPTs are computed by solving the collective Schrödinger equation with triaxial quadrupole shape degrees of freedom. The ingredients of the quadrupole collective Hamiltonian (QCH), that is, the deformation-dependent moments of inertia and mass parameters, and the collective potential, are determined by using the SCMF solutions as the microscopic inputs. Diagonalization of the QCH yields excitation spectra of low-energy positive-parity states and electric quadrupole and monopole transition rates. The RHB method that is combined with the QCH (denoted hereafter as RHB+QCH) has been employed in a number of previous theoretical investigations to predict

and describe a variety of nuclear structure phenomena [24, 31, 34, 41, 50–53].

The paper is organized as follows. In Sec. II, we outline the RHB+QCH approach. In Sec. III we present the SCMF results on the triaxial quadrupole potential energy surfaces, and the spectroscopic results on the low-energy excitation spectra, and $E2$ and $E0$ transition strengths. In the same section, we also show fluctuations of the β and γ deformations as another indicator of the phase transition. A special attention is given to the nucleus ^{82}Kr , recently suggested to be an empirical realization of the E(5) symmetry, and a detailed comparison with the experimental and E(5) spectra is made. Finally, Sec. IV gives a summary of the main results and conclusions.

II. THEORETICAL FRAMEWORK

In this section, we give a brief description of the RHB+QCH approach adopted for the present theoretical analysis. For the detailed account of the formalism and numerical machinery in the constrained RHB framework, the reader is referred to Refs. [30, 31, 54, 55], while the procedure to build the QCH from the SCMF solutions within the RHB is well documented, e.g., in Refs. [31, 34].

The constraints imposed in the present SCMF calculations are on the expectation values of the mass quadrupole operators

$$\hat{Q}_{20} = 2z^2 - x^2 - y^2 \quad \text{and} \quad \hat{Q}_{22} = x^2 - y^2, \quad (1)$$

which are related to the axially-symmetric deformation β and triaxiality γ [56], i.e.,

$$\beta = \sqrt{\frac{5}{16\pi} \frac{4\pi}{3} \frac{1}{A(r_0 A^{1/3})^2} \sqrt{\langle \hat{Q}_{20} \rangle^2 + 2 \langle \hat{Q}_{22} \rangle^2}}, \quad (2)$$

$$\gamma = \arctan \sqrt{2} \frac{\langle \hat{Q}_{22} \rangle}{\langle \hat{Q}_{20} \rangle}, \quad (3)$$

with $r_0 = 1.2$ fm. The calculations are carried out in a harmonic oscillator basis, with the number of oscillator shells equal to 20. The separable pairing force of finite range, originally developed in Ref. [49], includes two sets of parameters that are determined so as to reproduce the pairing gaps resulting from the Gogny D1 and D1S effective interactions. Throughout this paper, the parametrization associated with the D1S force is employed, that is, the pairing strength $V_0 = 728$ MeV fm³ and the parameter $a = 0.644$ fm of the Gaussian function entering the separable interaction, for both the proton and neutron pairings. The constrained RHB calculations provide the potential energy surfaces (see Fig. 1) and the SCMF single-particle solutions, which are subsequently used as the microscopic inputs to specify the collective Hamiltonian by the procedure described below.

Quadrupole collective states are provided as the solutions of the triaxial QCH, with the deformation-dependent parameters determined by the constrained

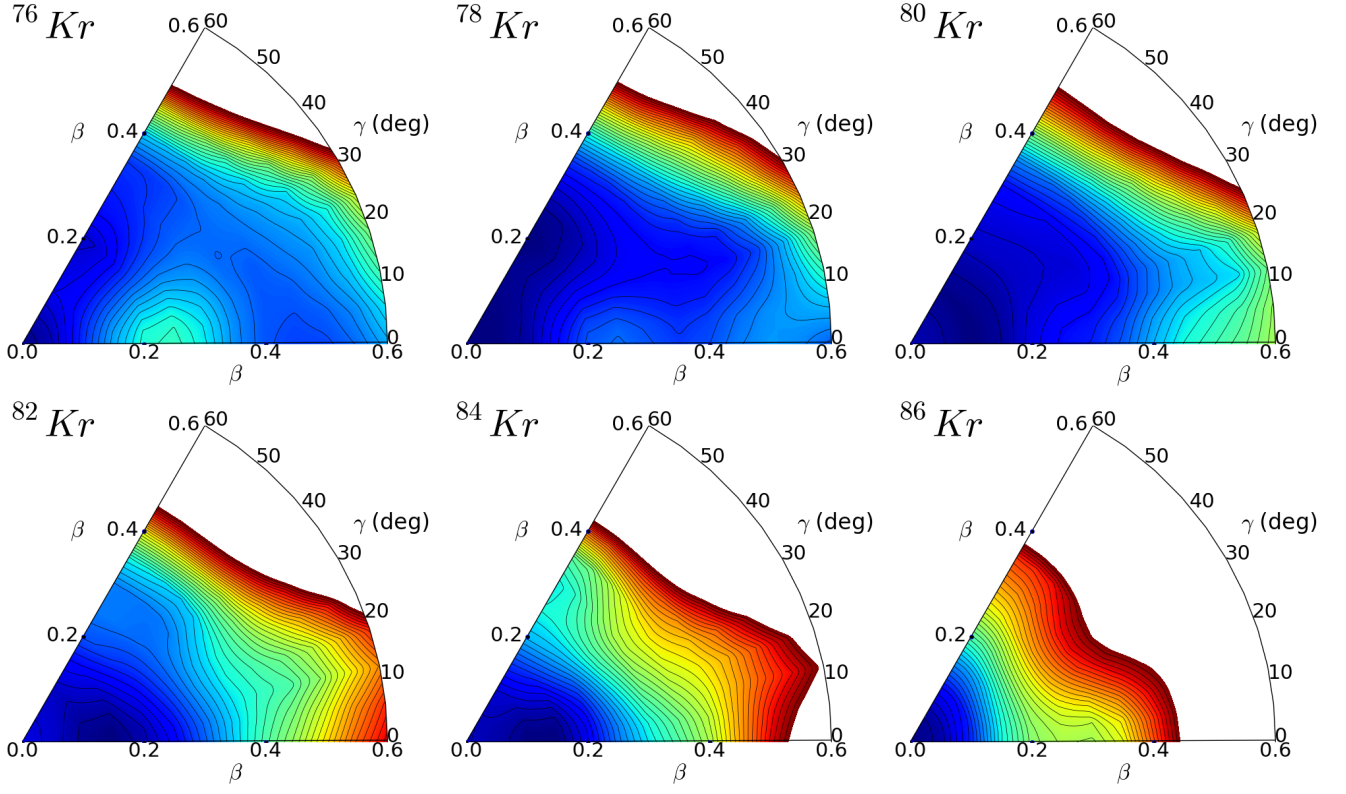


FIG. 1. Triaxial quadrupole potential energy surfaces for the even-even nuclei $^{76-86}\text{Kr}$ in terms of the β and γ deformation variables, computed by the constrained SCMF calculations within the RHB framework based on the relativistic functional DD-ME2 and the separable pairing force of finite range. The total SCMF energies are plotted up to 10 MeV from the global minimum, and the energy difference between neighboring contours is 250 keV.

SCMF calculation within the RHB framework. The QCH is given by

$$\hat{H}_{\text{coll}} = \hat{T}_{\text{vib}} + \hat{T}_{\text{rot}} + V_{\text{coll}}, \quad (4)$$

with the vibrational kinetic energy:

$$\begin{aligned} \hat{T}_{\text{vib}} = & -\frac{\hbar^2}{2\sqrt{wr}} \left[\frac{1}{\beta^4} \left(\frac{\partial}{\partial \beta} \sqrt{\frac{r}{w}} \beta^4 B_{\gamma\gamma} \frac{\partial}{\partial \beta} \right. \right. \\ & \left. \left. - \frac{\partial}{\partial \beta} \sqrt{\frac{r}{w}} \beta^3 B_{\beta\gamma} \frac{\partial}{\partial \gamma} \right) + \frac{1}{\beta \sin 3\gamma} \left(-\frac{\partial}{\partial \gamma} \sqrt{\frac{r}{w}} \sin 3\gamma \right. \right. \\ & \left. \left. \times B_{\beta\gamma} \frac{\partial}{\partial \beta} + \frac{1}{\beta} \frac{\partial}{\partial \gamma} \sqrt{\frac{r}{w}} \sin 3\gamma B_{\beta\beta} \frac{\partial}{\partial \gamma} \right) \right], \quad (5) \end{aligned}$$

and rotational kinetic energy:

$$\hat{T}_{\text{rot}} = \frac{1}{2} \sum_{k=1}^3 \frac{\hat{J}_k^2}{\mathcal{I}_k}, \quad (6)$$

where \hat{J}_k denotes the components of the angular momentum in the body-fixed frame of a nucleus. The moments of inertia \mathcal{I}_k , as well as the mass parameters $B_{\beta\beta}$, $B_{\beta\gamma}$, and $B_{\gamma\gamma}$, depend on the quadrupole deformation variables β and γ in such a way that $\mathcal{I}_k =$

$4B_k\beta^2 \sin^2(\gamma - 2k\pi/3)$. Two additional quantities that appear in the expression for the vibrational energy, i.e., $r = B_1 B_2 B_3$, and $w = B_{\beta\beta} B_{\gamma\gamma} - B_{\beta\gamma}^2$, determine the volume element in the collective space. The moments of inertia are computed using the Inglis-Belyaev (IB) formula [57, 58], and the mass parameters associated with the two quadrupole collective coordinates $q_0 = \langle \hat{Q}_{20} \rangle$ and $q_2 = \langle \hat{Q}_{22} \rangle$ are calculated in the cranking approximation. The collective potential V_{coll} in Eq. (4) is obtained by subtracting the zero-point energy corrections from the total RHB deformation energy.

The corresponding eigenvalue problem is solved using an expansion of eigenfunctions in terms of a complete set of basis functions that depend on the deformation variables β and γ , and the Euler angles $\Omega = (\phi, \theta, \psi)$. The diagonalization of the Hamiltonian yields the excitation energies and collective wave functions for each value of the total angular momentum and parity, that are used to calculate observables. Note that the present QCH approach is limited up to those spins at which the first band crossing takes place. The higher-spin states can be described by alternative approaches, e.g., by cranking models. Illustrative examples are found in Ref. [59], dealing with the $^{72,74,76}\text{Kr}$ nuclei.

An important advantage of using the collective model based on SCMF single-(quasi)particle solutions is the fact that physical observables, such as transition probabilities and spectroscopic quadrupole moments, are calculated in the full configuration space and there is no need for effective charges. Using the bare value of the proton charge in the electric quadrupole operator, the transition probabilities between eigenvectors of the collective Hamiltonian can be directly compared with data.

III. RESULTS AND DISCUSSION

A. Potential energy surfaces

Figure 1 shows contour plots of the triaxial quadrupole potential energy surfaces for the $^{76-86}\text{Kr}$ nuclei defined in terms of the axial deformation β and triaxiality γ . Only the results obtained by using the functional DD-ME2 are shown in the figure, because there is essentially no striking difference between the topology of the energy surfaces for the DD-ME2 and DD-PC1 EDFs. In Fig. 1, for $^{76,78}\text{Kr}$, we observe that in addition to a (nearly) spherical global minimum there is also an oblate local minimum around $\beta \approx 0.2$ on their energy surfaces. The spherical global minimum for ^{76}Kr is separated distinctly from the oblate minimum, and reflects the neutron $N = 40$ sub-shell closure. There occurs a third minimum around $\beta = 0.5$ on the prolate axis. For ^{78}Kr , the potential looks softer along the oblate $\gamma = 60^\circ$ axis, on which the global minimum is identified at $\beta \approx 0.05$ and the oblate local minimum at $\beta \approx 0.2$. For ^{80}Kr , the potential becomes almost completely flat in γ deformation, characteristic of the γ -unstable $O(6)$ symmetry of the IBM [7]. Both for ^{80}Kr and ^{82}Kr , a weakly prolate deformed shape is suggested, for which the potential is still considerably flat in γ direction and is soft also in the β deformation. The softness implies that the fluctuations are large and that a significant degree of shape mixing is present in the vicinity of the ground state. Finally, an approximate harmonic oscillator potential with the global minimum at $\beta = 0$ is obtained for ^{86}Kr . This is expected, since this nucleus corresponds to the neutron magic number $N = 50$.

B. Systematics of low-energy spectra

The discussion so far about the variation of the potential energy surface gives an approximate description of the shape QPT at the SCMF level, in analogy to the Landau theory of phase transitions. A more quantitative discussion about the QPTs should, therefore, involve the direct calculations of the spectroscopic properties that can be considered quantum order parameters. In the following, we consider overall behaviors of the excitation spectra and electric transition probabilities along the studied Kr chain.

Figure 2 shows the calculated excitation spectra for the low-lying quadrupole collective states of the $^{76-86}\text{Kr}$ nuclei, obtained within the RHB+QCH method. The results obtained with both functionals, DD-ME2 and DD-PC1 EDFs, are shown, while there appears to be no significant qualitative or quantitative difference between the two functionals in the prediction of energy spectra. For comparison, the figure also includes the corresponding experimental data [12, 60]. The RHB+QCH calculation provides a reasonable description of the experimental excitation energies of the 2_1^+ , 4_1^+ , 0_2^+ , and 2_2^+ states for the Kr isotopes with the neutron numbers $40 \leq N \leq 44$. Both the calculated and observed 0_2^+ excitation energy for the $N \approx 40$ nuclei is so low as to be about the same order of magnitude as the first excited state 2_1^+ . The calculation slightly underestimates the experimental 0_2^+ level. The low-lying 0_2^+ state near the neutron sub-shell gap $N = 40$ is often considered a signature of shape coexistence [14]. In our model calculation, a competition between a nearly spherical global, an oblate and an prolate local minima is suggested to occur in the SCMF triaxial quadrupole energy maps for ^{76}Kr and ^{78}Kr (see Fig. 1). For all those states shown in Fig. 2, the predicted excitation energies turn to increase abruptly from $N = 44$ to 46, and overestimate the data. As we approach the neutron major shell gap $N = 50$, both the calculated and experimental energy levels become higher with N . The energy levels of the non-yrast states 0_2^+ and 2_2^+ are here predicted to be particularly higher than the experimental ones for $N = 48$ and 50. Since the collective Hamiltonian gives purely collective states, the description of those nuclei close to the magic numbers becomes worse, in which nuclei single-particle excitations play a more relevant role.

The collective wave function, resulting from the diagonalization of the QCH, provides an insight into the nature of a given low-lying state. Of particular interest is ^{76}Kr , for which three competing mean-field minima occur in the potential energy surface (see Fig. 1). Figure 3 shows contour plots of the collective wave functions in the β - γ deformation plane corresponding to the 0_1^+ , 2_1^+ , 4_1^+ , 0_2^+ , 2_2^+ , and 0_3^+ states. The 0_1^+ wave function is spread over an area from the oblate to prolate sides, and exhibits a peak that is close to the oblate axis. The 2_1^+ wave function is, on the other hand, more sharply peaked on the prolate side with the deformation $\beta \approx 0.5$, around which the prolate local minimum occurs in the potential energy surface. The same is true for the 4_1^+ state and those with higher spin, $I > 4$, of the ground-state band. This result implies a transition from the nearly oblate to prolate configurations at low spin within the ground-state band, and thus the higher-spin members of the band are supposed to be made mainly of the strongly deformed prolate configurations. This finding is consistent with the conclusion drawn from the earlier cranking RHB calculation of Ref. [59]. The distribution of the 0_2^+ wave function in the β - γ surface indicates a distinct coexistence between the oblate and prolate shapes. The

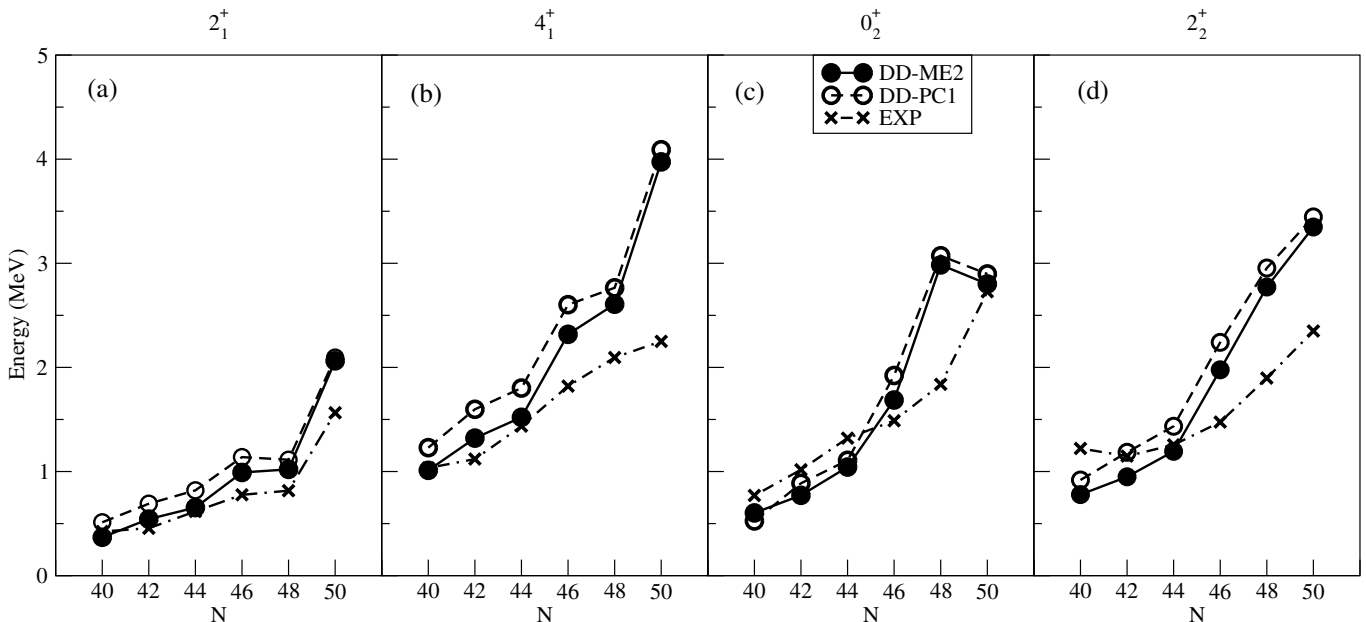


FIG. 2. Evolution of calculated and experimental low-energy spectra for the (a) 2_1^+ , (b) 4_1^+ , (c) 0_2^+ , and (d) 2_2^+ states for the even-even $^{76-86}\text{Kr}$ isotopes as functions of the neutron number N . The calculated results with both the DD-ME2 and DD-PC1 functionals are shown. The experimental data are taken from Refs. [12, 60].

2_2^+ state is suggested to be made largely of the triaxial configurations around $\gamma = 30^\circ$. One observes essentially three peaks in the 0_3^+ wave function distribution, which are associated with the weakly triaxially deformed, and the nearly oblate and prolate deformed configurations.

In addition, it is meaningful to study the sensitivity of the predicted excitation spectra to the pairing strength. A global study of the separable pairing force within the covariant density functional framework in Ref. [61] indicated that, in order to account for the empirical odd-even mass staggering, the strength of the separable pairing force needs to be modified so that it is scaled by particle-number dependent factors. We have then carried out the RHB+QCH calculation in which both the proton and neutron pairing strengths are scaled with the factors introduced in Eqs. (13–17) of Ref. [61]. For the ^{76}Kr and ^{82}Kr isotopes, for example, this modification gives rise to an increase of the pairing strengths by approximately 15%, if the parameters listed in Table I in that reference are adopted. For both of these nuclei, the RHB+QCH calculation employing the increased pairing strengths gives excitation spectra for all the states that are systematically larger than those obtained when the original pairing strength $V_0 = 728 \text{ MeV fm}^3$ is employed. Thus, in this particular case, the use of the pairing strength that is increased according to the prescription of Ref. [61] does not appear to improve the description of the excitation energies.

C. Systematics of $B(E2)$ transition rates

In Fig. 4 we show the results for the $B(E2)$ rates for the electric quadrupole transitions between the low-lying states, i.e., $B(E2; 2_1^+ \rightarrow 0_1^+)$, $B(E2; 4_1^+ \rightarrow 2_1^+)$, $B(E2; 0_2^+ \rightarrow 2_1^+)$, and $B(E2; 2_2^+ \rightarrow 2_1^+)$. The RHB+QCH calculation reproduces the experimental data for the $B(E2; 2_1^+ \rightarrow 0_1^+)$ and $B(E2; 4_1^+ \rightarrow 2_1^+)$ rates fairly well. The decreasing pattern of the $B(E2; 2_1^+ \rightarrow 0_1^+)$ and $B(E2; 4_1^+ \rightarrow 2_1^+)$ values suggests the weakening of the quadrupole collectivity towards the neutron magic number $N = 50$. For those nuclei with $40 \leq N \leq 44$, the present calculation suggests much stronger interband $E2$ transitions $0_2^+ \rightarrow 2_1^+$ and $2_2^+ \rightarrow 2_1^+$ than the experimental data. This result further confirms that a high degree of shape mixing is present near the ground state of these nuclei, especially ^{76}Kr and ^{78}Kr : the corresponding SCMF potential energy surfaces are notably soft in both the β and γ deformations, and indicate the coexistence of the three minima (see Fig. 1). While the energy levels of the 0_2^+ [Fig. 2(c)] and 2_2^+ [Fig. 2(d)] states are reasonably described, the interband $E2$ transitions appear to be rather sensitive to the relevant wave functions. One can see in Fig. 3, for instance, a substantial overlap between the 2_1^+ and 2_2^+ collective wave functions in ^{76}Kr , which can result in the too enhanced $2_2^+ \rightarrow 2_1^+$ transition as compared to the experimental value. For the $N \geq 46$ nuclei, on the other hand, we observe that the calculated $B(E2; 0_2^+ \rightarrow 2_1^+)$ and $B(E2; 2_2^+ \rightarrow 2_1^+)$ values [Figs. 4(c) and 4(d)] rapidly decrease from $N = 44$ to 46, and are consistent with the experimental values. Note, however,

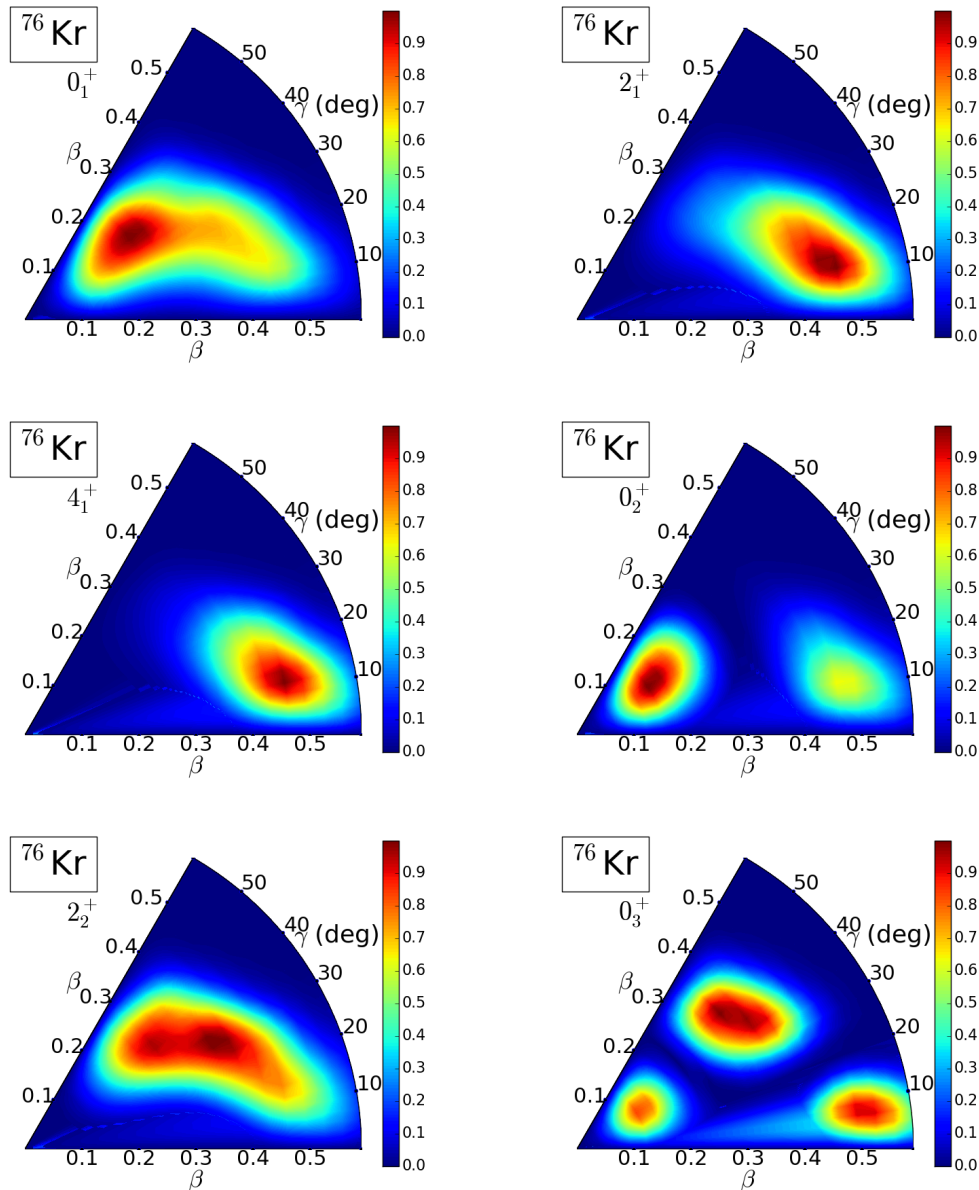


FIG. 3. Distributions of the collective wave functions for the 0_1^+ , 2_1^+ , 4_1^+ , 0_2^+ , 2_2^+ , and 0_3^+ states of ^{76}Kr in the $\beta - \gamma$ plane obtained from the diagonalization of the QCH. The functional DD-ME2 is used.

that the decrease of the interband $B(E2)$ rates is also considered a consequence of the fact that the quadrupole collectivity becomes weaker as the neutron major shell closure $N = 50$ is approached.

The calculated results for the $B(E2)$ transition rates based on the two EDFs, DD-ME2 and DD-PC1, are basically similar to each other both at the qualitative and quantitative levels. A notable difference, however, arises in the prediction of the $B(E2; 0_2^+ \rightarrow 2_1^+)$ values at $N = 40$, for which the DD-PC1 EDF leads to about twice as large a value as the DD-ME2 EDF.

D. $E0$ transitions

Let us consider the monopole transition properties of the studied Kr nuclei. Figure 5 shows the calculated $\rho^2(E0)$ values for the $E0$ transitions $0_2^+ \rightarrow 0_1^+$ and $0_3^+ \rightarrow 0_1^+$. The $\rho^2(E0; 0_2^+ \rightarrow 0_1^+)$ values are here calculated to be considerably larger than the experimental values [62], while the observed decreasing pattern from $N = 42$ to 46 is reproduced by our model calculation. The large $E0$ transition strengths, especially for the Kr nuclei with $N = 40 - 44$, corroborates the strong shape mixing between the wave functions of the low-lying 0^+

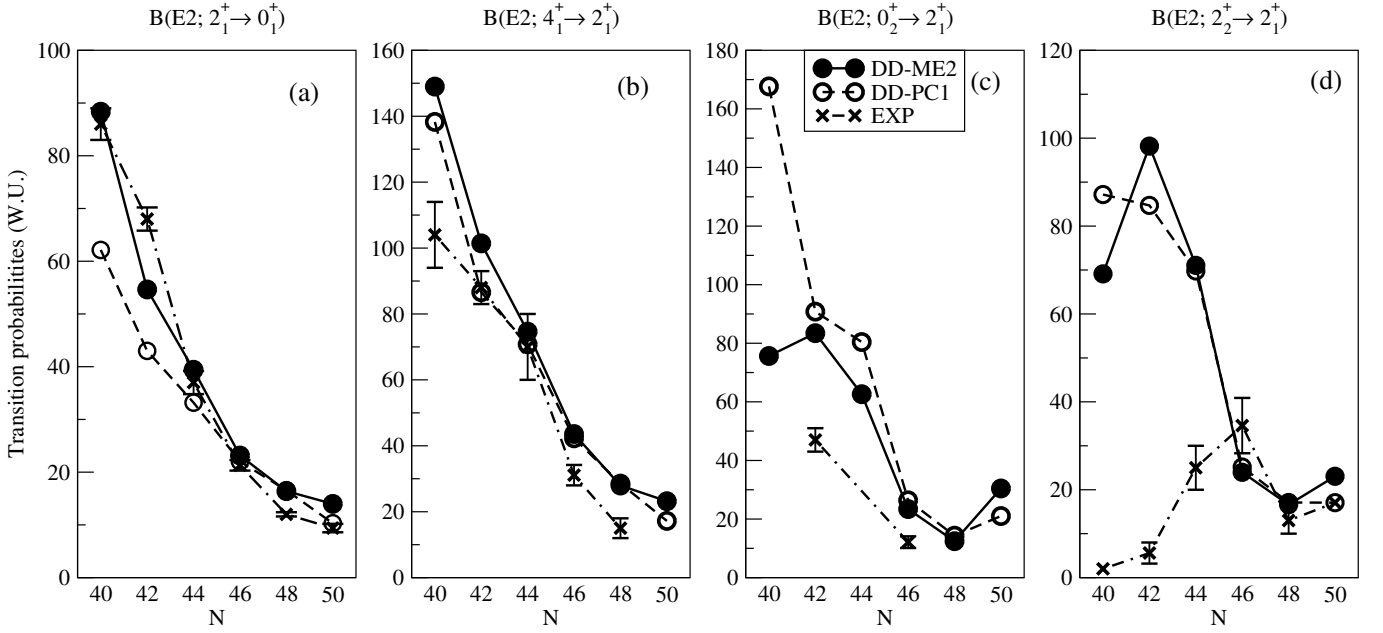


FIG. 4. Evolution of calculated and experimental $B(E2)$ strengths in Weisskopf units (W.u.) for the transitions (a) $2_1^+ \rightarrow 0_1^+$, (b) $4_1^+ \rightarrow 2_1^+$, (c) $0_2^+ \rightarrow 2_1^+$, and (d) $2_2^+ \rightarrow 2_1^+$ for the even-even $^{76-86}\text{Kr}$ isotopes as functions of N . Theoretical results based on the DD-ME2 and DD-PC1 EDFs are shown. The experimental data are taken from Ref. [12] for ^{82}Kr and from Ref. [60] otherwise.

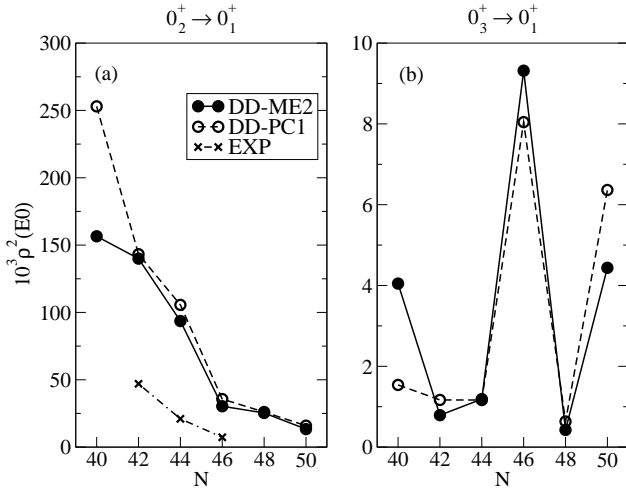


FIG. 5. Calculated and experimental $\rho^2(E0; 0_2^+ \rightarrow 0_1^+)$ and $\rho^2(E0; 0_3^+ \rightarrow 0_1^+)$ values for the $^{76-86}\text{Kr}$ nuclei. The experimental values are taken from Ref. [62].

states. See in Fig. 3 a significant overlap between the 0_1^+ and 0_2^+ collective functions for ^{76}Kr . It is worth noticing that there appears a sudden decrease of the calculated $\rho^2(E0; 0_2^+ \rightarrow 0_1^+)$ value from $N = 44$ to 46 , implying a rapid nuclear structure change. As seen in Fig. 5(b), in the present calculation the $\rho^2(E0; 0_3^+ \rightarrow 0_1^+)$ value is by more than two orders of magnitude smaller than the

$\rho^2(E0; 0_2^+ \rightarrow 0_1^+)$ one, and hence no large overlap between the 0_3^+ and the 0_1^+ ground state is expected to be present. Similarly to the $B(E2)$ results, the most notable difference between the theoretical $\rho^2(E0; 0_3^+ \rightarrow 0_1^+)$ values obtained from the two EDFs appears at $N = 40$.

E. Signatures of shape phase transitions

We have seen in the previous sections that the RHB+QCH calculation provides a fairly reasonable description of the observed low-energy spectra, $B(E2)$, and $\rho^2(E0)$ values. Let us now turn to analyze several spectroscopic properties that can serve as a more distinct signature of the QPT, especially, in comparison with various symmetry limits of the IBM and E(5). Such an analysis also presents a sensitive test of the employed model.

1. Energy ratios

Figure 6 shows ratios of the calculated excitation energies of low-lying states for the considered $^{76-86}\text{Kr}$ nuclei. The ratio $R_{4/2} \equiv E(4_1^+)/E(2_1^+)$ is a typical indicator that distinguishes among various geometrical limits for the nuclear shapes. In Fig. 6(a) the calculated ratio $R_{4/2}$ exhibits a weak parabolic dependence on N , with a minimum value at $N = 44$. In most of the nuclei, the calculated $R_{4/2}$ ratio is approximately in between the E(5) limit, $R_{4/2} = 2.20$, and the γ -unstable O(6) limit of the

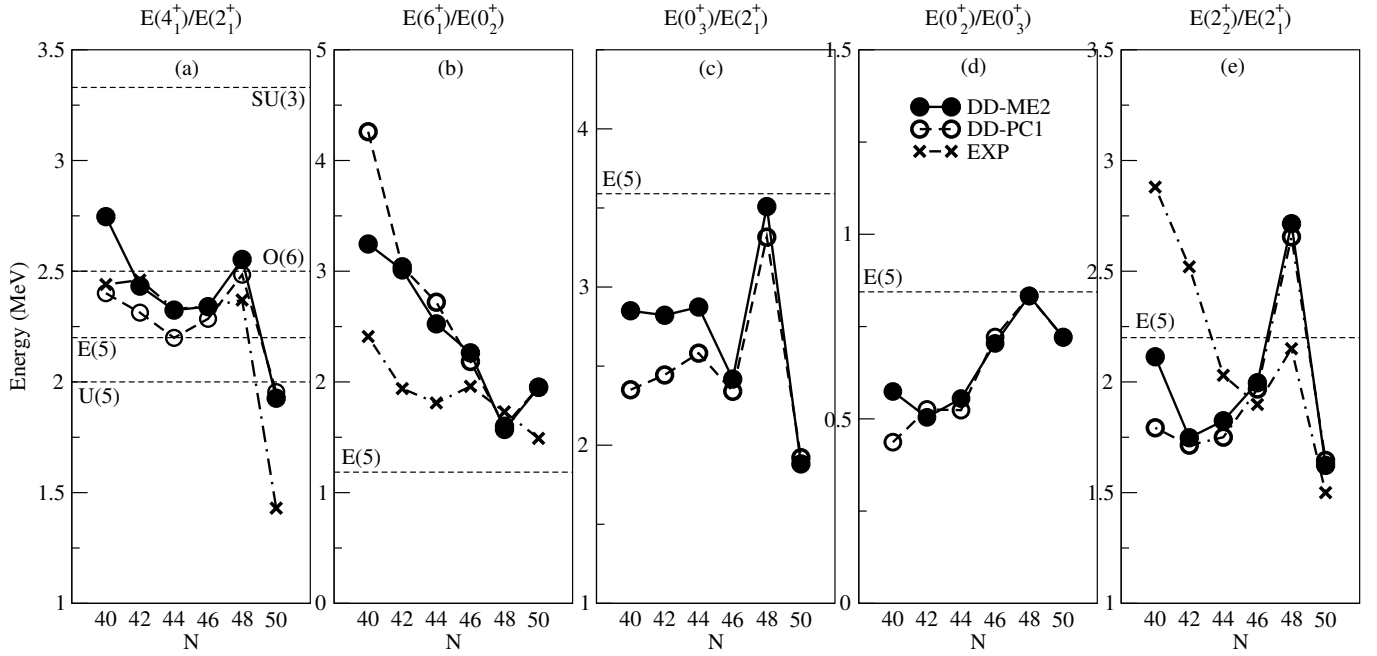


FIG. 6. Evolution of calculated and experimental energy ratios (a) $E(4_1^+)/E(2_1^+)$, (b) $E(6_1^+)/E(0_2^+)$, (c) $E(0_3^+)/E(2_1^+)$, (d) $E(0_2^+)/E(0_3^+)$, and (e) $E(2_2^+)/E(2_1^+)$ for the even-even $^{76-86}\text{Kr}$ isotopes as functions of N . The calculated results with both the DD-ME2 and DD-PC1 functionals are shown, in comparison to the limits of the E(5) symmetry and three dynamical symmetries of the IBM.

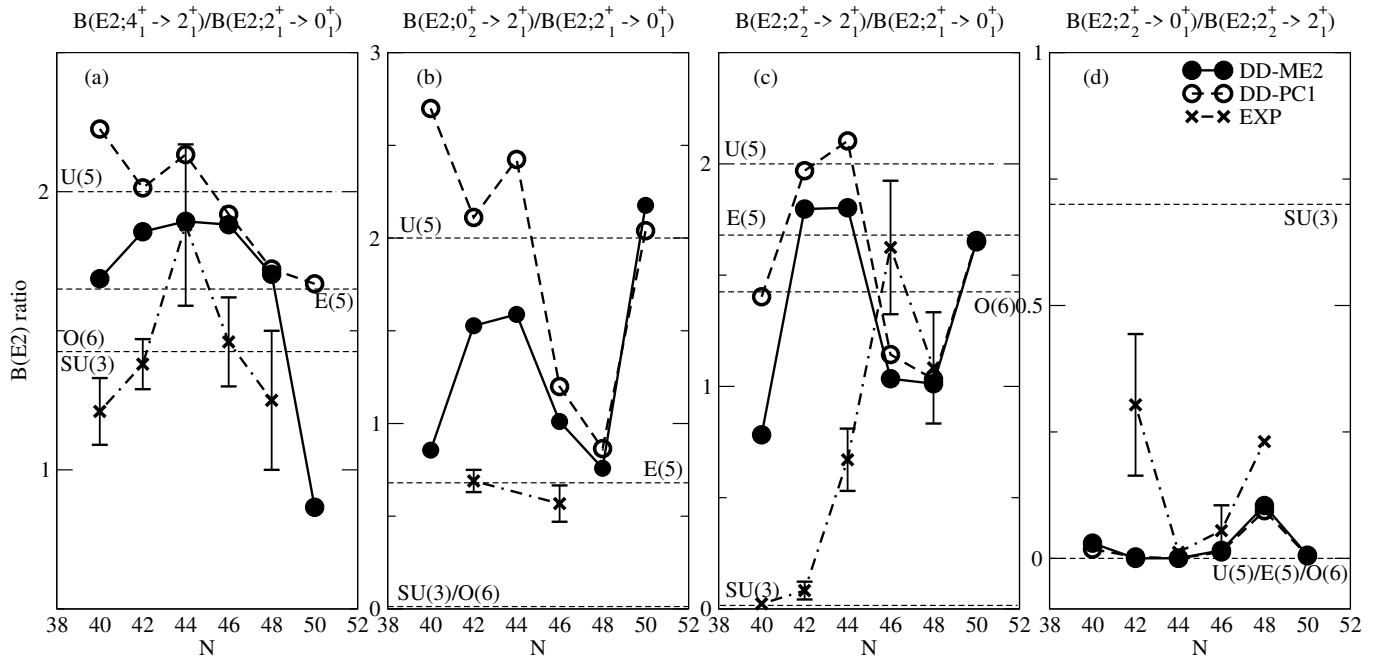


FIG. 7. Evolution of calculated and experimental ratios of the $B(E2)$ transition rates, (a) $R_1 = B(E2; 4_1^+ \rightarrow 2_1^+)/B(E2; 2_1^+ \rightarrow 0_1^+)$, (b) $R_2 = B(E2; 0_2^+ \rightarrow 2_1^+)/B(E2; 2_1^+ \rightarrow 0_1^+)$, (c) $R_3 = B(E2; 2_2^+ \rightarrow 2_1^+)/B(E2; 2_1^+ \rightarrow 0_1^+)$, and (d) $R_4 = B(E2; 2_2^+ \rightarrow 0_1^+)/B(E2; 2_2^+ \rightarrow 2_1^+)$, for the $^{76-86}\text{Kr}$ isotopes. The values predicted by the dynamical symmetries of the IBM (U(5), SU(3), and O(6)) and the E(5) CPS are also indicated. The experimental data are taken from Ref. [12, 60]

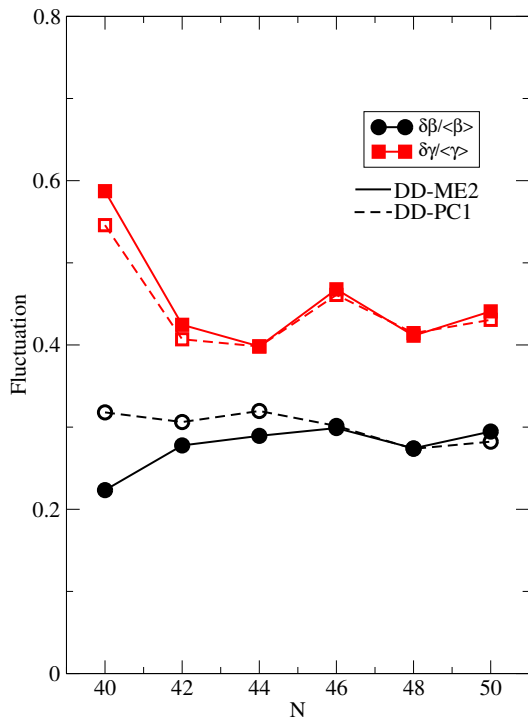


FIG. 8. Fluctuations of the β and γ deformations for $^{76-86}\text{Kr}$, computed by using the QCH wave function of the 0_1^+ ground state for each nucleus based on the DD-ME2 and DD-PC1 EDFs.

IBM, $R_{4/2} = 2.5$ [7]. For both EDFs, the $R_{4/2}$ values for ^{80}Kr and ^{82}Kr in the RHB+QCH calculation appear to be close to the E(5) limit $R_{4/2} = 2.20$.

In Fig. 6(b) the observed energy ratio $R_{6/0} \equiv E(6_1^+)/E(0_2^+)$ gradually decreases with N , approaching the E(5) limit 1.19. The calculated values with both EDFs show a similar, but a more rapid change with N . This trend also conforms to the shape evolution into γ -soft deformation in the studied Kr nuclei.

In Fig. 6(c), the energy ratio $R_{0/2} \equiv E(0_3^+)/E(2_1^+)$ is shown. For most of the nuclei the RHB+QCH calculation provides smaller values than the E(5) limit $R_{0/2} = 3.59$. The calculation with the DD-ME2 EDF gives larger $R_{0/2}$ ratios for $40 \leq N \leq 44$. The calculation, however, suggests an irregular behavior of $R_{0/2}$ from $N = 46$ to 50. This is mostly because both the 2_1^+ and 0_3^+ excitation energies are here overestimated, especially as the neutron number increases towards the $N = 50$ neutron magic number (see Fig. 2(a)).

Figure 6(d) shows the ratio $R_{0/0} \equiv E(0_2^+)/E(0_3^+)$, which provides information about relative locations of the first and second excited 0^+ levels. The calculated ratio $R_{0/0} = 0.704$ (or 0.721) in the case of the DD-ME2 (or DD-PC1) EDF for ^{82}Kr is in a fair agreement with the E(5) limit, $R_{0/0} = 0.84$, and with the experimental data, 0.9 [12]. From Fig. 6(d) the calculated $R_{0/0}$ values for ^{84}Kr and ^{86}Kr are also close to the E(5) limit. How-

ever, this is simply because the $0_{2,3}^+$ excitation energies for these nearly spherical nuclei are not satisfactorily described by the collective Hamiltonian, and should not be considered a signature of the E(5) symmetry.

The energy ratio $R_{2/2} \equiv E(2_2^+)/E(2_1^+)$ indicates the location of the γ -vibrational band, with the 2_2^+ state being the bandhead, relative to the ground-state $K = 0_1^+$ band. As shown in Fig. 6(e), the calculated $R_{2/2}$ ratios underestimate the experimental data for the region $40 \leq N \leq 44$, while the isotopic dependence looks more or less similar between the theory and experiment. The predicted value $R_{2/2} = 2.00$ (or 1.97) with the DD-ME2 (or DD-PC1) EDF is close to both the experimental data, 1.90, and the E(5) limit, 2.20.

2. $B(E2)$ ratios

Next, we consider the ratios of the calculated $B(E2)$ transition rates:

$$R_1 = B(E2; 4_1^+ \rightarrow 2_1^+)/B(E2; 2_1^+ \rightarrow 0_1^+), \quad (7)$$

$$R_2 = B(E2; 0_2^+ \rightarrow 2_1^+)/B(E2; 2_1^+ \rightarrow 0_1^+), \quad (8)$$

$$R_3 = B(E2; 2_2^+ \rightarrow 2_1^+)/B(E2; 2_1^+ \rightarrow 0_1^+), \quad (9)$$

$$R_4 = B(E2; 2_2^+ \rightarrow 0_1^+)/B(E2; 2_2^+ \rightarrow 2_1^+). \quad (10)$$

The corresponding results are shown in Fig. 7, and are compared with the U(5), SU(3), and O(6) limits of the IBM, and the E(5) [8] limit. Note that the three IBM limits shown in the figure are obtained in the large-boson-number limit [7].

As seen in Fig. 7(a), the R_1 ratios obtained here are approximately in between the U(5) vibrational limit, $R_1 = 2.0$, and the E(5) limit, $R_1 = 1.68$. Both functionals lead to systematically larger R_1 values than the experimental ones, except for ^{80}Kr in the case of the DD-ME2 result. The calculation with DD-ME2 EDF generally produces the R_1 values closer to the data than with the DD-PC1. The systematic trend of the R_1 ratio with N in the DD-ME2 case also looks more or less similar to the experimental one, i.e., an inverse parabolic dependence on N centered around $N = 44$.

The calculated R_2 ratios are shown in Fig. 7(b). The experimental data are available only for the ^{78}Kr and ^{82}Kr nuclei. As anticipated by the strong $0_2^+ \rightarrow 2_1^+$ transitions [cf. Fig. 4(c)], the present RHB+QCH calculation overestimates the experimental R_2 ratios by several factors for these nuclei. The ratio R_2 also seems to be quite sensitive to the choice of the EDFs for $40 \leq N \leq 44$. In particular, the calculation with the DD-ME2 EDF generally yields a smaller R_2 ratio, hence closer to the experimental value, than with the DD-PC1. Both EDFs produce rather small R_2 values for ^{82}Kr and ^{84}Kr . Especially for the former nucleus, our calculation gives $R_2 = 1.01$ (or 1.20) with the DD-ME2 (or DD-PC1) functional, while the experimental and E(5) values are $R_2 = 0.57 \pm 0.10$ and $R_2 = 0.68$, respectively.

Figure 7(c) shows the results for the R_3 ratio. Experimentally, this quantity appears to reflect the structural evolution from the SU(3) rotational limit at $N = 40$ and 42 to the γ -unstable O(6) or E(5) limit at $N = 46$. Concerning the $^{76-80}\text{Kr}$ nuclei, the calculated R_3 ratios are much larger than the data, and are also quite far from the SU(3) limit $R_3 = 0$. The large finite R_3 ratios for these nuclei further confirm the enhanced shape mixing in the present theoretical framework, as is shown in Fig. 1 that the SCMF potential energy surfaces have coexisting mean-field minima for $^{76,78}\text{Kr}$ and are totally flat in the γ direction for ^{80}Kr . As a consequence, the overlap between the resultant wave functions for the low-spin states is supposed to be large, leading to the unexpectedly strong $2_2^+ \rightarrow 2_1^+$ $E2$ transitions for the $^{76-80}\text{Kr}$ nuclei. Probably the low-lying structures of these nuclei are so complicated that the simple QCH approach combined with a particular choice of the underlying EDF and pairing interaction may not necessarily give a reasonable agreement with the empirical data. For those nuclei with $N \geq 46$, however, the predicted R_3 ratios agree rather well with the experimental data. Note that the value for ^{82}Kr has a large error bar.

The R_4 ratio particularly distinguishes the deformed rotor limit SU(3) from the O(6) and U(5) ones. As seen in Fig. 6(d), the present calculation provides, for most of the Kr nuclei, nearly vanishing values of R_4 . Our results agree with the data for $^{80,82,84}\text{Kr}$, but not for ^{78}Kr . For the latter nucleus, a large finite value $R_4 = 0.30 \pm 0.14$ has been observed experimentally [60]. The vanishing R_4 ratio obtained by our calculation for the $N \leq 44$ nuclei reflects that the corresponding $B(E2; 2_2^+ \rightarrow 2_1^+)$ rates are calculated to be considerably large due to the strong configuration mixing [see Fig. 4(d)].

3. Fluctuations in shape variables

As yet another signature of the QPT in the Kr isotopes, we consider the fluctuations for the β and γ deformations, defined respectively as $\delta\beta/\langle\beta\rangle$ and $\delta\gamma/\langle\gamma\rangle$. Here,

$$\delta\beta = \frac{\sqrt{\langle\beta^4\rangle - \langle\beta^2\rangle^2}}{2\langle\beta\rangle}, \quad (11)$$

$$\delta\gamma = \left(\sqrt{\frac{\langle\beta^6 \cos^2 3\gamma\rangle}{\langle\beta^6\rangle}} - \sqrt{\frac{\langle\beta^3 \cos 3\gamma\rangle^2}{\langle\beta^4\rangle\langle\beta^2\rangle}} \right) \times (3 \sin 3\langle\gamma\rangle)^{-1}, \quad (12)$$

stand for the deviation, and

$$\langle\beta\rangle = \sqrt{\langle\beta^2\rangle} \quad (13)$$

$$\langle\gamma\rangle = \arccos\left(\langle\beta^3 \cos 3\gamma\rangle / \sqrt{\langle\beta^4\rangle\langle\beta^2\rangle}\right) / 3 \quad (14)$$

are the average values of the β and γ deformations, respectively. The above quantities are computed by using

the wave function for the 0_1^+ ground state. The fluctuations in the deformation variables have also been considered in previous EDF-based calculations for the studies, e.g., of the spherical to γ -soft shape transitions in Ba and Xe nuclei in the mass $A \approx 130$ region [24], and of the quadrupole-octupole shape phase transitions in a wider mass region [46]. A discontinuity of the fluctuations when plotted as functions of the nucleon number is considered a signature of the QPT.

Figure 8 shows the corresponding results obtained from both the DD-ME2 and DD-PC1 EDFs. We see that, regardless of the choice of the EDF, the fluctuation in the γ deformation $\delta\gamma/\langle\gamma\rangle$ exhibits a notable kink at $N = 46$, signaling the occurrence of the QPT. There also appears a significant decrease of the γ fluctuation from $N = 40$ to 42, indicating the effect of the neutron sub-shell closure $N = 40$. According to the SCMF results presented in Fig. 1, the potential energy surface for ^{80}Kr is almost completely flat in the γ deformation, while the global prolate minimum at $\beta \approx 0.15$ appears for ^{82}Kr . In Fig. 8 the fluctuation in the axial deformation β , $\delta\beta/\langle\beta\rangle$, shows a minor kink at $N = 46$, when the DD-ME2 EDF is chosen. In general, however, the fluctuation in the axial deformation $\delta\beta/\langle\beta\rangle$ shows only a gradual variation with N , and is not considered as distinct a signature as the one for the triaxial deformation $\delta\gamma/\langle\gamma\rangle$.

4. Detailed level structure

Let us look into a more detailed energy-level structure of individual nuclei. Here we specifically consider the transitional nuclei ^{82}Kr and ^{80}Kr , since particularly the former has been suggested [12] to be a candidate for the E(5) critical-point nucleus. The triaxial RHB energy surface for the nucleus ^{82}Kr indeed exhibits a flat-bottomed potential that weakly depends on the γ deformation (see Fig. 1), and that most closely resembles the E(5) potential.

A well-known fact is that the moments of inertia computed by using the IB formula are considerably smaller than the empirical values. In order to effectively take into account this deficiency, the IB moments of inertia have often been increased by $\approx 30 - 40\%$ in many of the previous calculations using collective Hamiltonian (see, e.g., Ref. [24]). In the same spirit, and in order to make a meaningful comparison between the theoretical and experimental energy spectra, we show, in this particular section, the spectroscopic results for ^{82}Kr and ^{80}Kr obtained from the QCH calculation with the IB moment of inertia increased by 40%. The effect of the increase is such that excitation energies for all the states, except for the 0^+ ones, are lowered by approximately 10 – 30%.

Note also that the $2_{\xi=1,\tau=1}^+$ energy level and $B(E2; 2_{\xi=1,\tau=1}^+ \rightarrow 0_{\xi=1,\tau=0}^+)$ value in the E(5) spectrum are normalized to the experimental [12, 60] 2_1^+ levels and $B(E2; 2_1^+ \rightarrow 0_1^+)$ values, respectively, where ξ and τ are quantum numbers of E(5) [8].

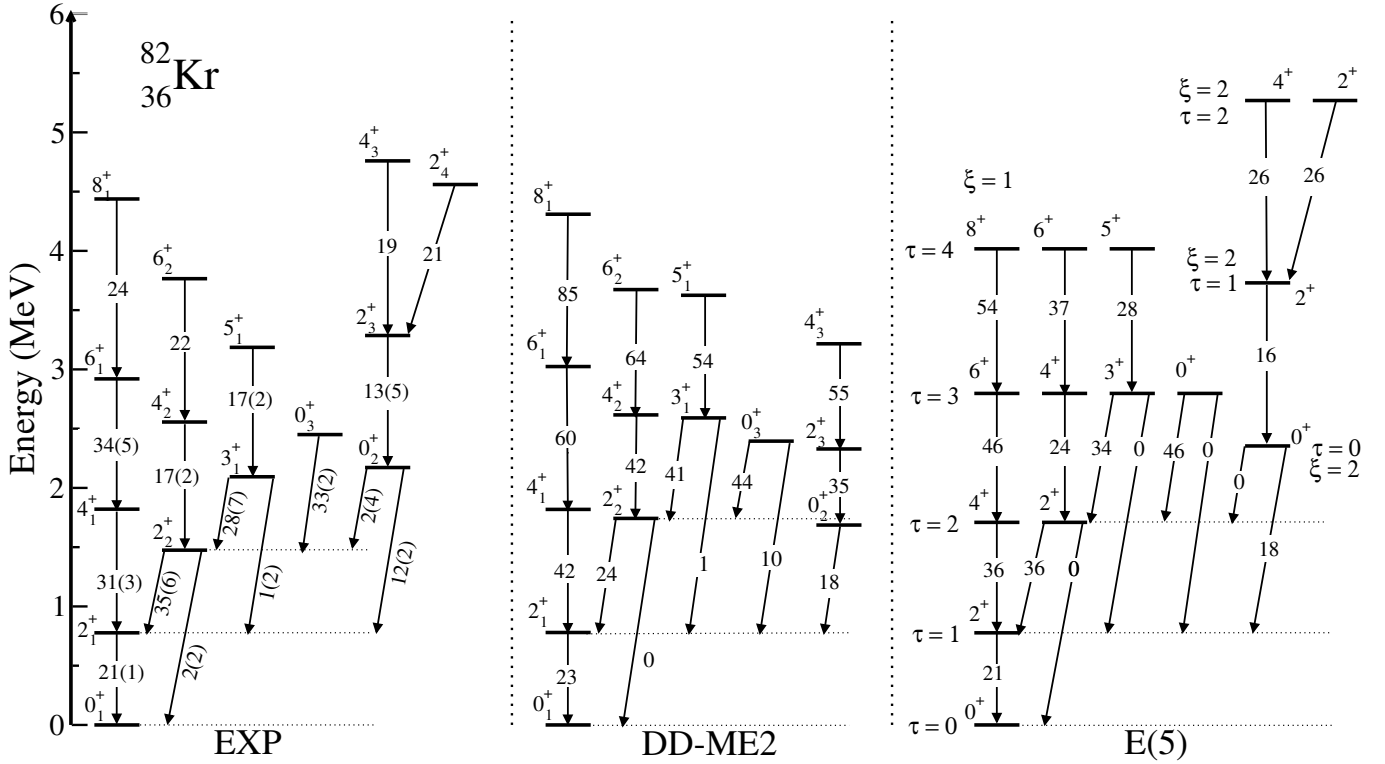


FIG. 9. Comparison of experimental, calculated, and E(5) energy spectra and $B(E2)$ transition strengths (in W.u.) for the ^{82}Kr nucleus. The functional DD-ME2 is used for the theoretical spectrum. Note that, in the QCH calculation, the IB moments of inertia are increased by 40 %. The experimental data are taken from Ref. [12]. In the E(5) spectrum, quantum numbers labelling states ξ and τ are shown, and the excitation energy of the state $2_{\xi=1, \tau=1}^+$ and the $B(E2; 2_{\xi=1, \tau=1}^+ \rightarrow 0_{\xi=1, \tau=0}^+)$ rate are normalized to the corresponding experimental $E(2_1^+)$ excitation energy and $B(E2; 2_1^+ \rightarrow 0_1^+)$ value [12], respectively.

Figure 9 shows the computed excitation spectra and $B(E2)$ transition strengths for ^{82}Kr , obtained from the RHB+QCH method that uses the DD-ME2 EDF, in comparison to the corresponding experimental and E(5) energy spectra. One notices that the present calculation reproduces the overall feature of the experimental energy spectrum. The calculated $B(E2)$ transition rates within the ground-state, $K = 0_1^+$ band are generally larger than the experimental values. Especially, the calculation gives increasing inband $E2$ transition strength as a function of the angular momentum within the $K = 0_1^+$ band, and this systematic trend disagrees with the data but agrees with E(5).

The quasi- γ , or $K = 2_\gamma^+$ band here comprises the 2_2^+ , 3_1^+ , 4_2^+ , 5_1^+ , and 6_2^+ states. The energy level of the 2_2^+ bandhead state is predicted to be below that of the 4_1^+ state, which is a typical feature of the γ -soft nucleus and is also consistent with the empirical trend. The RHB+QCH result, however, indicates a staggering pattern that is characterized by the near degeneracy of the even- and odd-spin members of the band, i.e., $(3_\gamma^+, 4_\gamma^+)$, $(5_\gamma^+, 6_\gamma^+)$, \dots . This energy-level pattern is consistent with the E(5) symmetry, and is characteristic of the γ -unstable rotor model [63], or, equivalently, the O(6) symmetry of

the IBM. In addition, the calculated $K = 2_\gamma^+$ band exhibits the $E2$ selection rule for the interband transitions to the $K = 0_1^+$ band in agreement with the experimental data and E(5).

The 0_3^+ state in the present RHB+QCH calculation is here associated with the $0_{1,3}^+$ state of E(5). The calculated 0_3^+ excitation energy is close to the experimental data, but is rather lower than the corresponding $0_{1,3}^+$ level of E(5). The nearly vanishing $B(E2; 0_3^+ \rightarrow 2_2^+)/B(E2; 0_3^+ \rightarrow 2_1^+)$ branching ratio is here obtained, consistently with the experimental data and with the selection rule of E(5).

Our model further predicts the $K = 0_2^+$ band consisting of the 0_2^+ , 2_3^+ , 4_3^+ , \dots states, which is associated with part of the $\xi = 2$ family in the E(5) spectrum. An overall feature of the calculated $K = 0_2^+$ looks similar to that of the experimental counterpart. The $B(E2; 0_2^+ \rightarrow 2_1^+)$ value is here computed to be 18 W.u., in a fair agreement with both the experimental value and $B(E2; 0_{2,0}^+ \rightarrow 2_{1,1}^+)$ rate of E(5). However, the calculated $K = 0_2^+$ band is considerably lower in energy than the observed one and $\xi = 2$ band of E(5). Especially, the energy level of the bandhead state 0_2^+ is here predicted to be below the 2_2^+ level, which disagrees with the data and E(5). A pre-

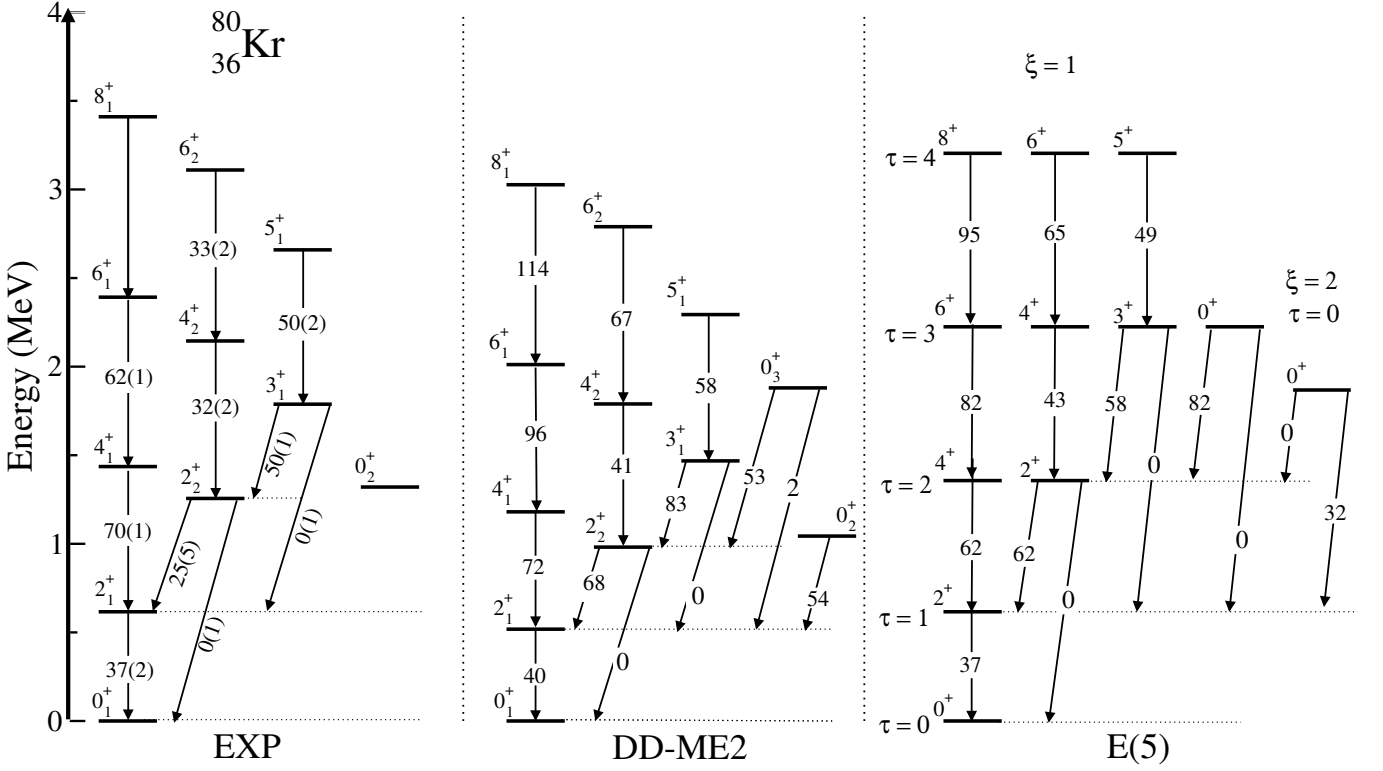


FIG. 10. Same as Fig. 9, but for the ^{80}Kr nucleus. The experimental data are taken from Ref. [60].

vious five-dimensional collective Hamiltonian calculation based on the HFB method using the Gogny D1S EDF [36] obtained the 0_2^+ excitation energy for the ^{82}Kr isotopes, that is slightly lower than the 2_2^+ one. In the symmetry-projected triaxial GCM calculation also using the Gogny-D1S EDF [42], the 0_2^+ energy level was predicted to be lower than the 2_2^+ one for ^{82}Kr .

In Fig. 10 we make a similar comparison for the adjacent nucleus ^{80}Kr . As we can see in Fig. 1, the corresponding SCMF energy surface for ^{80}Kr is almost flat in the γ direction, which is a manifestation of the O(6) symmetry. Figure 10 shows that the energy spectrum calculated for ^{80}Kr by the RHB+QCH model is, qualitatively, in a better agreement with the experimental data than in the case of ^{82}Kr . The calculated spectrum is, however, generally more compressed than the experimental one. As compared to the E(5) spectrum, both the calculated and experimental 0_2^+ energy levels are much lower than the corresponding $0_{2,0}^+$ one. In contrast to ^{82}Kr , we obtain for ^{80}Kr a weak $E2$ transition, $B(E2; 0_2^+ \rightarrow 2_2^+) = 0.11$ W.u. This conforms to the E(5) selection rule, which forbids the $E2$ transition $0_{2,0}^+ \rightarrow 2_{1,2}^+$.

In the third column of Table I the calculated energy and $B(E2)$ ratios of low-lying states of the ^{82}Kr nucleus, obtained with the DD-ME2 EDF, are shown. The results are compared with the corresponding experimental values [12] (the second column) and E(5) limits [8]

(last column). In the table, the states are labelled by the E(5) quantum numbers as $0_{1,0}^+$, $2_{1,1}^+$, $4_{1,2}^+$, $2_{1,2}^+$, $0_{2,0}^+$, and $0_{1,3}^+$, which are, respectively, associated with the 0_1^+ , 2_1^+ , 4_1^+ , 2_2^+ , 0_2^+ , and 0_3^+ states in the calculation as well as the experiment. Of particular interest are the properties of the excited 0^+ states. We notice that the ratio $E(0_{2,0}^+)/E(2_{1,1}^+)$ in our calculation is considerably smaller than the E(5) value, 3.03. The $E2$ selection rule for the $0_{1,3}^+$ state of E(5), i.e., $\frac{B(E2; 0_{1,3}^+ \rightarrow 2_{1,1}^+)}{B(E2; 0_{1,3}^+ \rightarrow 2_{1,2}^+)} = 0$ is reasonably accounted for in our model. On the other hand, we obtain a large branching ratio $\frac{B(E2; 0_{2,0}^+ \rightarrow 2_{1,2}^+)}{B(E2; 0_{2,0}^+ \rightarrow 2_{1,1}^+)} = 2.98$, which disagree with the data and with E(5). Note that the $0_{2,0}^+ \rightarrow 2_{1,2}^+$ transition is here predicted to be particularly strong, i.e., $B(E2; 0_2^+ \rightarrow 2_2^+) = 55$ W.u..

The results for ^{80}Kr are shown in the fifth column of Table I. Both the theoretical and experimental $E(0_{2,0}^+)/E(2_{1,1}^+)$ ratios are considerably smaller than the E(5) value. The predicted ratio $E(0_{1,3}^+)/E(2_{1,1}^+) = 3.63$ for ^{80}Kr is here suggested to be closer to the E(5) value, 3.59, than for ^{82}Kr . It is worthwhile to remark that, in accordance with the E(5) selection rules for the $E2$ transitions, the present calculation gives nearly vanishing values for both the $\frac{B(E2; 0_{2,0}^+ \rightarrow 2_{1,2}^+)}{B(E2; 0_{2,0}^+ \rightarrow 2_{1,1}^+)}$ and $\frac{B(E2; 0_{1,3}^+ \rightarrow 2_{1,1}^+)}{B(E2; 0_{1,3}^+ \rightarrow 2_{1,2}^+)}$ ratios. The result for the former branching ratio is in a marked contrast to the one for ^{82}Kr . Nevertheless, since

TABLE I. Calculated and experimental energy and $B(E2)$ ratios for low-lying states of the transitional nuclei ^{82}Kr and ^{80}Kr , and the corresponding E(5) limits. The states are labelled by the E(5) quantum numbers ξ and τ . The DD-ME2 EDF is used for the calculation. The experimental data for ^{82}Kr and ^{80}Kr are taken from Refs. [12] and [60], respectively, while the E(5) values are taken from [8].

Ratio	^{82}Kr		^{80}Kr		E(5)
	Experiment	DD-ME2	Experiment	DD-ME2	
$E(4_{1,2}^+)/E(2_{1,1}^+)$	2.34	2.33	2.33	2.28	2.20
$E(0_{2,0}^+)/E(2_{1,1}^+)$	2.80	2.16	2.14	2.01	3.03
$E(0_{1,3}^+)/E(2_{1,1}^+)$	3.2	3.07		3.63	3.59
$E(0_{2,0}^+)/E(0_{1,3}^+)$	0.9	0.70		0.55	0.84
$E(2_{1,2}^+)/E(2_{1,1}^+)$	1.90	2.00	2.04	1.82	2.20
$B(E2; 4_{1,2}^+ \rightarrow 2_{1,1}^+)$					
$B(E2; 2_{1,1}^+ \rightarrow 0_{1,0}^+)$	1.48 ± 0.16	1.81	1.88 ± 0.29	1.82	1.68
$B(E2; 2_{1,2}^+ \rightarrow 2_{1,1}^+)$	1.67 ± 0.30	1.09	0.67 ± 0.14	1.75	1.68
$B(E2; 2_{1,1}^+ \rightarrow 0_{1,0}^+)$					
$B(E2; 0_{2,0}^+ \rightarrow 2_{1,1}^+)$	0.57 ± 0.10	0.80		1.38	0.86
$B(E2; 2_{1,1}^+ \rightarrow 0_{1,0}^+)$					
$B(E2; 0_{2,0}^+ \rightarrow 2_{1,2}^+)$	0.2 ± 0.3	2.98		0.0020	0
$B(E2; 0_{2,0}^+ \rightarrow 2_{1,1}^+)$					
$B(E2; 0_{1,3}^+ \rightarrow 2_{1,1}^+)$	0.1 ± 0.1	0.22		0.036	0
$B(E2; 0_{1,3}^+ \rightarrow 2_{1,2}^+)$					

the experimental information about the low-lying states of ^{80}Kr is not as abundant as for ^{82}Kr , an extensive comparison between the RHB+QCH result and experiment is difficult.

IV. CONCLUDING REMARKS

Based on the framework of the nuclear density functional theory, we have investigated the spectroscopic properties that signal the shape-phase transitions in the chain of the Kr isotopes in the mass $A \approx 80$ region, with a particular focus on the ^{82}Kr nucleus, which was recently identified as empirical evidence for the E(5) CPS. The constrained SCMF calculations within the RHB method using two representative classes of the relativistic EDF and a pairing interaction have been performed for the even-even nuclei $^{76-86}\text{Kr}$. The SCMF solutions have been then used as the microscopic inputs to determine the ingredients of the five-dimensional quadrupole collective Hamiltonian, that is, the deformation-dependent moments of inertia and mass parameters, and the collective potential. The diagonalization of the QCH has yielded excitation spectra and transition probabilities of the considered Kr nuclei.

The resultant triaxial quadrupole deformation energy surfaces have indicated an evolution of the equilibrium shape as a function of the nucleon number (Fig. 1): a competition among a nearly spherical global, an oblate, and a strongly prolate deformed local minima in $^{76,78}\text{Kr}$, a notable γ -softness in ^{80}Kr , a weakly-deformed prolate shape characterized by a flat-bottomed potential that is soft both in the β and γ deformations for $^{82,84}\text{Kr}$, and a nearly spherical shape for ^{86}Kr , corresponding to the

neutron major shell closure $N = 50$. The RHB+QCH calculation has provided a reasonable description of the experimental low-energy spectra (Fig. 2) for $N \leq 44$, but overestimates the data for $N \geq 46$ as the neutron magic number $N = 50$ is approached. Around the shell closure, the QCH approach, which produces purely collective states, is not expected to give a very good description of the empirical data. The calculated $B(E2)$ rates (Fig. 4) have been shown to be generally in agreement with the data, whereas particularly the $2_2^+ \rightarrow 2_1^+$ transition strengths for $N \leq 44$ have been overestimated, due to the strong shape mixing.

The behaviors of the calculated energy and $B(E2)$ ratios, and fluctuations in β and γ deformations along the isotopic chain have indicated the underlying nuclear structural change around ^{82}Kr , characterized by the significant amount of shape mixing. The detailed analyses of the calculated low-energy spectra of the transitional nuclei ^{82}Kr and ^{80}Kr have been made in comparison to the experimental and E(5) spectra (cf. Figs. 9 and 10). Particularly for ^{82}Kr , the predicted quasi- γ , $K = 2_\gamma^+$ band has been shown to be higher than the experimental one, in such a way that the bandhead 2_2^+ level is close in energy to the 4_1^+ one in the ground-state band. Another notable deviation from the experiment as well as from the E(5) symmetry appears in the description of the 0_2^+ energy level, which is here calculated to be so low as to be below the 2_2^+ one for ^{82}Kr , and which shows the $E2$ branching ratio that is quite at variance with the experimental data and E(5). The deviation from the data has arisen in part from the particular choice of the EDFs, which may further point to some deficiencies of the model when it is applied to this particular mass region. Another possibility consists in the fact that

the employed RHB+QCH approach in its current version presents a relatively simple model, which is built on the triaxial quadrupole shape degrees of freedom only, and thus the inclusions of some additional collective degrees of freedom in the Hamiltonian, in a similar spirit, e.g., to Refs. [64–66], may improve the description of the data. It is an interesting future study to investigate these possibilities.

In conclusion, the RHB+QCH method has demonstrated an ability to provide the spectroscopic observables that can be directly comparable to the experimental data, based solely on a choice of the universal EDF and pairing interaction. The approach allows for a timely, systematic and computationally feasible theoretical prediction for the nuclear shape-related phenomena that are experimentally of much interest, such as the

shape QPTs and coexistence, and is expected to serve as a useful benchmark for more complicated microscopic calculations.

ACKNOWLEDGMENTS

The authors are grateful to Antonio Bjelčić for helping them with implementation of the modified RHB solver. This work is financed within the Tenure Track Pilot Programme of the Croatian Science Foundation and the École Polytechnique Fédérale de Lausanne, and the Project TTP-2018-07-3554 Exotic Nuclear Structure and Dynamics, with funds of the Croatian-Swiss Research Programme.

-
- [1] P. Cejnar and J. Jolie, *Prog. Part. Nucl. Phys.* **62**, 210 (2009).
- [2] P. Cejnar, J. Jolie, and R. F. Casten, *Rev. Mod. Phys.* **82**, 2155 (2010).
- [3] L. Carr, ed., *Understanding Quantum Phase Transitions* (CRC Press, 2010).
- [4] F. Iachello, *Rivista del Nuovo Cimento* **34**, 617 (2011).
- [5] P. Cejnar and P. Stránský, *Phys. Scr.* **91**, 083006 (2016).
- [6] L. Fortunato, *Prog. Part. Nucl. Phys.* **121**, 103891 (2021).
- [7] F. Iachello and A. Arima, *The interacting boson model* (Cambridge University Press, Cambridge, 1987).
- [8] F. Iachello, *Phys. Rev. Lett.* **85**, 3580 (2000).
- [9] F. Iachello, *Phys. Rev. Lett.* **87**, 052502 (2001).
- [10] R. F. Casten and N. V. Zamfir, *Phys. Rev. Lett.* **85**, 3584 (2000).
- [11] R. F. Casten, *Prog. Part. Nucl. Phys.* **62**, 183 (2009).
- [12] S. Rajbanshi, S. Bhattacharyya, R. Raut, R. Palit, S. Ali, R. Santra, H. Pai, F. S. Babra, R. Banik, S. Bhattacharyya, P. Dey, G. Mukherjee, M. S. R. Laskar, S. Nandi, T. Trivedi, S. S. Ghugre, and A. Goswami, *Phys. Rev. C* **104**, L031302 (2021).
- [13] J. L. Wood, K. Heyde, W. Nazarewicz, M. Huyse, and P. van Duppen, *Phys. Rep.* **215**, 101 (1992).
- [14] E. Clément, A. Gørgen, W. Korten, E. Bouchez, A. Chatillon, J.-P. Delaroche, M. Girod, H. Goutte, A. Hüerstel, Y. L. Coz, A. Obertelli, S. Péru, C. Theisen, J. N. Wilson, M. Zielinska, C. Andreoiu, F. Becker, P. A. Butler, J. M. Casandjian, W. N. Catford, T. Czosnyka, G. d. France, J. Gerl, R.-D. Herzberg, J. Iwanicki, D. G. Jenkins, G. D. Jones, P. J. Napiorkowski, G. Sletten, and C. N. Timis, *Phys. Rev. C* **75**, 054313 (2007).
- [15] J. Ljungvall, A. Gørgen, M. Girod, J.-P. Delaroche, A. Dewald, C. Dossat, E. Farnea, W. Korten, B. Melon, R. Menegazzo, A. Obertelli, R. Orlandi, P. Petkov, T. Pissulla, S. Siem, R. P. Singh, J. Srebrny, C. Theisen, C. A. Ur, J. J. Valiente-Dobón, K. O. Zell, and M. Zielinska, *Phys. Rev. Lett.* **100**, 102502 (2008).
- [16] K. Heyde and J. L. Wood, *Rev. Mod. Phys.* **83**, 1467 (2011).
- [17] D. Bonatsos, I. E. Assimakis, N. Minkov, A. Martinou, R. B. Cakirli, R. F. Casten, and K. Blaum, *Phys. Rev. C* **95**, 064325 (2017).
- [18] A. Martinou, D. Bonatsos, T. J. Mertzimekis, K. E. Karakatsanis, I. E. Assimakis, S. K. Peroulis, S. Sarantopoulou, and N. Minkov, *Eur. Phys. J. A* **57**, 84 (2021).
- [19] N. Shimizu, T. Otsuka, T. Mizusaki, and M. Honma, *Phys. Rev. Lett.* **86**, 1171 (2001).
- [20] E. Caurier, G. Martínez-Pinedo, F. Nowacki, A. Poves, and A. P. Zuker, *Rev. Mod. Phys.* **77**, 427 (2005).
- [21] T. Togashi, Y. Tsunoda, T. Otsuka, and N. Shimizu, *Phys. Rev. Lett.* **117**, 172502 (2016).
- [22] N. Shimizu, T. Abe, M. Honma, T. Otsuka, T. Togashi, Y. Tsunoda, Y. Utsuno, and T. Yoshida, *Phys. Scr.* **92**, 063001 (2017).
- [23] T. Nikšić, D. Vretenar, G. A. Lalazissis, and P. Ring, *Phys. Rev. Lett.* **99**, 092502 (2007).
- [24] Z. P. Li, T. Nikšić, D. Vretenar, and J. Meng, *Phys. Rev. C* **81**, 034316 (2010).
- [25] K. Nomura, D. Vretenar, T. Nikšić, and B.-N. Lu, *Phys. Rev. C* **89**, 024312 (2014).
- [26] K. Nomura, R. Rodríguez-Guzmán, and L. M. Robledo, *Phys. Rev. C* **96**, 064316 (2017).
- [27] L. M. Robledo, T. R. Rodríguez, and R. R. Rodríguez-Guzmán, *J. Phys. G: Nucl. Part. Phys.* **46**, 013001 (2019).
- [28] J.-P. Ebran, M. Girod, E. Khan, R. D. Lasserri, and P. Schuck, *Phys. Rev. C* **102**, 014305 (2020).
- [29] N. Schunck, ed., *Energy Density Functional Methods for Atomic Nuclei* (IOP Publishing, 2019).
- [30] D. Vretenar, A. V. Afanasjev, G. A. Lalazissis, and P. Ring, *Phys. Rep.* **409**, 101 (2005).
- [31] T. Nikšić, D. Vretenar, and P. Ring, *Prog. Part. Nucl. Phys.* **66**, 519 (2011).
- [32] M. Bender, P.-H. Heenen, and P.-G. Reinhard, *Rev. Mod. Phys.* **75**, 121 (2003).
- [33] P. Ring and P. Schuck, *The Nuclear Many-Body Problem* (Springer-Verlag, Berlin, 1980).
- [34] T. Nikšić, Z. P. Li, D. Vretenar, L. Próchniak, J. Meng, and P. Ring, *Phys. Rev. C* **79**, 034303 (2009).
- [35] L. Próchniak and S. G. Rohoziński, *J. Phys. G: Nucl. Part. Phys.* **36**, 123101 (2009).
- [36] J. P. Delaroche, M. Girod, J. Libert, H. Goutte, S. Hilaire, S. Péru, N. Pillet, and G. F. Bertsch, *Phys. Rev. C*

- 81**, 014303 (2010).
- [37] K. Nomura, N. Shimizu, and T. Otsuka, *Phys. Rev. Lett.* **101**, 142501 (2008).
- [38] K. Nomura, N. Shimizu, and T. Otsuka, *Phys. Rev. C* **81**, 044307 (2010).
- [39] M. Bender, P. Bonche, and P.-H. Heenen, *Phys. Rev. C* **74**, 024312 (2006).
- [40] M. Girod, J.-P. Delaroche, A. Görgen, and A. Obertelli, *Phys. Lett. B* **676**, 39 (2009).
- [41] Y. Fu, H. Mei, J. Xiang, Z. P. Li, J. M. Yao, and J. Meng, *Phys. Rev. C* **87**, 054305 (2013).
- [42] T. R. Rodríguez, *Phys. Rev. C* **90**, 034306 (2014).
- [43] J. M. Yao, K. Hagino, Z. P. Li, J. Meng, and P. Ring, *Phys. Rev. C* **89**, 054306 (2014).
- [44] K. Nomura, R. Rodríguez-Guzmán, Y. M. Humadi, L. M. Robledo, and H. Abusara, *Phys. Rev. C* **96**, 034310 (2017).
- [45] H. Abusara and S. Ahmad, *Phys. Rev. C* **96**, 064303 (2017).
- [46] K. Nomura, L. Lotina, T. Nikšić, and D. Vretenar, *Phys. Rev. C* **103**, 054301 (2021).
- [47] G. A. Lalazissis, T. Nikšić, D. Vretenar, and P. Ring, *Phys. Rev. C* **71**, 024312 (2005).
- [48] T. Nikšić, D. Vretenar, and P. Ring, *Phys. Rev. C* **78**, 034318 (2008).
- [49] Y. Tian, Z. Y. Ma, and P. Ring, *Phys. Lett. B* **676**, 44 (2009).
- [50] V. Prassa, T. Nikšić, G. A. Lalazissis, and D. Vretenar, *Phys. Rev. C* **86**, 024317 (2012).
- [51] Z. P. Li, T. Nikšić, and D. Vretenar, *J. Phys. G: Nucl. Part. Phys.* **43**, 024005 (2016).
- [52] J. Xiang, Z. P. Li, W. H. Long, T. Nikšić, and D. Vretenar, *Phys. Rev. C* **98**, 054308 (2018).
- [53] V. Prassa and K. E. Karakatsanis, *Int. J. Mod. Phys. E* **30**, 2150054 (2021).
- [54] T. Nikšić, N. Paar, D. Vretenar, and P. Ring, *Comput. Phys. Commun.* **185**, 1808 (2014).
- [55] A. Bjelčić, T. Nikšić, and Z. Drmač, DIRHBSspeedup, <https://github.com/abjelcic/DIRHBSspeedup.git> (2021).
- [56] A. Bohr and B. R. Mottelson, *Nuclear Structure*, Vol. II (Benjamin, New York, USA, 1975).
- [57] D. R. Inglis, *Phys. Rev.* **103**, 1786 (1956).
- [58] S. Beliaev, *Nucl. Phys.* **24**, 322 (1961).
- [59] A. V. Afanasjev and S. Frauendorf, *Phys. Rev. C* **71**, 064318 (2005).
- [60] Brookhaven National Nuclear Data Center, <http://www.nndc.bnl.gov>.
- [61] S. Teeti and A. V. Afanasjev, *Phys. Rev. C* **103**, 034310 (2021).
- [62] T. Kibédi and R. Spear, *At. Data and Nucl. Data Tables* **89**, 77 (2005).
- [63] L. Wilets and M. Jean, *Phys. Rev.* **102**, 788 (1956).
- [64] J. Xiang, Z. P. Li, T. Nikšić, D. Vretenar, and W. H. Long, *Phys. Rev. C* **101**, 064301 (2020).
- [65] K. Nomura, D. Vretenar, Z. P. Li, and J. Xiang, *Phys. Rev. C* **102**, 054313 (2020).
- [66] K. Nomura, D. Vretenar, Z. P. Li, and J. Xiang, *Phys. Rev. C* **103**, 054322 (2021).